Development of Ar^{+16} charge exchange recombination spectroscopy measurements at ASDEX Upgrade

R. M. McDermott[1], R. Dux[1], F. Guzman[2], T. Pütterich[1], R. Fischer[1], A. Kappatou,[1] and the ASDEX Upgrade Team

[1] Max-Planck-Institut für Plasmaphysik, Boltzmannstr. 2, 85748 Garching, Germany
[2] Department of Physics and Astronomy, University of North Georgia, GA, USA

E-mail: Rachael.McDermott@ipp.mpg.de

Abstract. Argon is being considered as a radiator for future fusion devices. To support this, experiments in present day devices are needed to assess its effectiveness as a radiator and to study its compatibility with key aspects of reactor operation. For these purposes, accurate measurement of the Ar density in the confined plasma region are required. Charge exchange recombination spectroscopy (CXRS) is capable of providing this information, but requires validated cross-sections to produce accurate density profiles. For typical ASDEX Upgrade (AUG) plasma parameters Ar^{+16} is the charge state of the most interest and the ArXVI n=15-14 was identified as the best target for these measurements. Due to the fine structure splitting, the Ar charge exchange (CX) emission lines are highly asymmetric and detailed modeling is required to extract accurate ion temperatures or rotations. For the evaluation of Ar^{+16} densities, there are two main sets of CX cross-sections available: the data calculated by Schultz *et al* [1, 2] (ORNL) and by Errea *et al* [3] (UAM). These cross-sections differ by over an order of magnitude and have very different energy dependences. In this work, the validity of these datasets is tested experimentally. The Ar density profiles calculated using the ORNL cross-sections are 10-50× too large while the UAM densities are a factor of 2.73 too small. The UAM data, however, does a much better job at capturing the observed energy dependence. The authors conclude that the CTMC calculations of Errea, which use a hydrogenic distribution to describe the initial target and donor distributions better reproduce the experimental data. However, to produce accurate Ar density profiles, these cross-sections need to be corrected downward and the best profiles are produced with a small correction to the UAM energy dependence.

1. Introduction

One of the most difficult challenges facing magnetic confinement fusion is how to handle the high heat fluxes incident on the plasma facing components (PFC) inherent to burning plasma conditions. In present day devices, the PFCs and their accompanying cooling systems can, for typical operating conditions, cope with the incident heat fluxes. However, this will not be the case for future machines such as ITER or DEMO [4, 5, 6]. As such, additional radiative cooling schemes are foreseen to protect the PFCs and, in

particular, the divertor targets. As ITER is expected to operate only slightly above the H-mode power threshold, a high core radiated power fraction can not be tolerated. Therefore, in this device a lower-Z seed impurity, such as nitrogen, will be necessary to increase the radiated power fraction specifically in the divertor region. In DEMO or in an equivalent reactor prototype machine, however, this will not be sufficient. Additional core radiation will be required to handle the higher fusion-alpha produced heat fluxes. For this, slightly higher-Z seed impurities, such as argon, are being considered [7]. Experiments in present day devices using these seed impurities are necessary to assess their effectiveness as divertor and mantle radiators, study their transport in the plasma core, and their compatibility with key aspects of reactor operation. Of particular interest is the radiative cooling in the pedestal. Radiation is an actuator for control of the local pressure gradient and thus may become a key ingredient for the suppression of ELMs, which is regarded as mandatory for DEMO. Therefore, integration of no-ELM scenarios with argon seeding is currently being investigated in ASDEX Upgrade [8].

These experiments require accurate measurements of the impurity densities in the confined plasma region. Charge exchange recombination spectroscopy (CXRS) can be used for this purpose and has advantages over other diagnostic techniques in that it can provide local measurements of individual charge states of the desired species [9, 10], opposed to line-integrated measurements of radiation from potentially multiple impurities and charge states. While CXRS with low-Z impurities ($Z<10$) is routinely used in tokamak plasmas to measure the impurity ion temperature, rotation, and densities, it is not a standard tool for medium- or high-Z impurities, although some exploration of CXRS on medium-Z elements has been performed, for example, on Ar [1] and Al [11]. There are several reasons why CXRS measurements are mainly performed on low-Z elements. First, low-Z impurities are typically fully stripped inside of the pedestal in fusion plasmas, making measurements of a single charge state sufficient to diagnose the behaviour of the impurity at all radii in the plasma. For higher-Z elements, however, multiple charge states exist, necessitating significantly more diagnostic coverage to monitor the complete plasma profile. Secondly, both Zeeman splitting and fine structure play stronger roles for higher-Z elements, complicating the interpretation of the measured spectra and the extraction of reliable temperature and rotation profiles. Thirdly, and perhaps most importantly, the charge exchange cross-sections for higher-Z elements are not as well known as their lower-Z counterparts and calculations for these elements are significantly more challenging owing, at least in part, to the need to include capture into higher-n states [12].

In the case of argon, the transitions of interest for visible charge exchange are from electrons in levels with principle quantum numbers n between 14 and 17 and calculations of the relevant cross-sections have resulted in atomic data-sets that span several orders of magnitude and display very different energy dependencies at relevant neutral beam injection (NBI) energies (ORNL: [1, 2], UAM: [3]). To make reliable argon charge exchange measurements usable emission lines in the visible that provide sufficient signal have to be identified and, for argon densities, the atomic data must be validated.

In Schlummer *et al* [13], work in this direction has been done for CX with H-like Ar (Ar^{+17}). Here, the available CX effective emission rates were compared against X-ray line measurements and it was found that the ORNL dataset was better able to describe the experimental data. For standard ASDEX Upgrade (AUG) plasma discharges, the charge state of the most interest is He-like Ar (Ar^{+16}), as it exists over most of the plasma minor radius. Only in the center of the plasma, where the temperature exceeds $\sim$ 2. keV, is the He-like Ar lost and either the H-like or fully stripped Ar must be measured to complete the radial profile. Therefore, the Ar^{+16} population has become the main workhorse for Ar CXRS measurements at AUG and is the main focus of this publication. Here we show that for CX with Ar^{+16} (Ar XVI n=15-14, 541.1 nm), neither the ORNL nor the UAM datasets produce accurate Ar density profiles. However, the UAM dataset recovers the correct order of magnitude and does a significantly better job of reproducing the observed energy dependence of the CX cross-sections.

In section 2 of this work, eight different Ar CX emission lines in the visible are explored. Example spectra and fits are shown for all and the best lines for charge exchange with Ar^{+16}, Ar^{+17}, and Ar^{+18} are identified. The apparent widths and positions resulting from fits to these spectra are strongly affected by both Zeeman and fine structure splitting, necessitating dedicated modeling to extract reliable temperatures and rotations. The methods for doing this are discussed and simplified correction curves that enable approximate temperatures and rotations to be easily produced are presented in section 2.1. In section 3 the available charge exchange cross-section data for CX with Ar^{+16} (Ar XVI n=15-14) are discussed and the experiments performed to test the accuracy of these cross-sections are presented in section 4. Finally, the impurity density analysis of the measured CXRS Ar intensities using both the ORNL and UAM datasets is presented in Sec. 5. The main results of this work are summarized in section 6.

2. Argon charge exchange lines in the visible

The charge exchange reaction can be written,

$$H + A^{Z+} \rightarrow H^{+} + A^{(Z-1)+}, \tag{1}$$

where a neutral atom (H) loses its electron to an ion (A) of charge Z, reducing its net charge to $Z-1$. After the reaction, the electron decays to lower energy levels, emitting line radiation with energies (wavelengths) characteristic of the '$Z-1$' population. The information contained in the resultant spectra, however, is reflective of the 'Z' population. To avoid confusion, in this work the emission lines will always be referred to using spectroscopic notation, while the population being measured is denoted by its charge. For example, for CX with He-like argon, the population is denoted Ar^{+16} while the corresponding emission is written as Ar XVI with the relevant n transition additionally identified.

In this work eight argon charge exchange lines have been explored with the aim of identifying the best emission lines for CXRS measurements of Ar^{+16}, Ar^{+17}, and Ar^{+18}.

These lines are listed in Table 1 and an example spectrum from each of them can be see in Figs. 1 and 2. All of the spectra shown in these figures were obtained in very similar plasma discharges with very similar argon content, except for the Ar XVI n=14-13 line shown in the top panel of Fig. 2. This emission line was measured only later in piggyback on another experiment and its intensity is, therefore, not directly comparable to the intensities of the other argon lines shown.

Ar Transition	Wavelength (nm)
Ar XVIII n=17-16	630.31197
Ar XVIII n=16-15	522.37757
Ar XVIII n=15-14	427.51797
Ar XVII n=16-15	585.65103
Ar XVII n =15-14	479.30282
Ar XVI n=16-15	661.15538
Ar XVI n=15-14	541.09773
Ar XVI n =14-13	436.52030

Table 1. Argon emission lines that have been measured in AUG discharges with the aim of identifying the best lines in the visible for providing reliable impurity ion temperature, rotation, and density profiles in the presence of argon seeding. The rest wavelengths provided correspond to the center of mass of the full Zeemen and fine structure split pattern.

For charge exchange with Ar^{+18} the XVIII n=16-15 transition was identified as the best available line. The emission from the XVIII n=15-14 transition, shown in the top left panel of Fig.1, has extremely low signal due to the very low transmission of the diagnostic in this wavelength region. In addition, there are two Ar II lines in the same spectral region, indicated by vertical dashed orange lines. The blue dashed lines correspond to Ar I lines. The wavelengths for these lines were taken from the NIST spectral line database. The XVIII n=17-16 emission line at 630.5 nm, shown in the bottom left panel of Fig. 1, is perturbed by a colder Ar line from a lower charge state (possibly Ar I) as well as multiple other smaller lines that can be seen in the background. These additional emissions complicate the fit and interpretation of the data. The XVIII n=16-15 transition (middle left panel), on the other hand, is better isolated and has the added benefit of being only 7 nm away from the standard carbon CX line at 529.05 nm (not shown). This enables the measurement of Ar^{+18} to be performed simultaneously with C^{+6}, as most of the AUG spectrometers image at least a 12 nm wavelength range [14, 15]. The red dashed lines in these figures show the individual Gaussians needed to (approximately) fit the data.

On the right hand side of Fig. 1 example spectra from the two Ar XVII (CX with Ar^{+17}) lines explored are shown. The Ar XVII n=15-14 emission at 479.5 nm can not be fit by a single Gaussian. The residuals indicate the presence of a second emission line. Indeed before argon is puffed in this discharge, a line can be seen in this wavelength

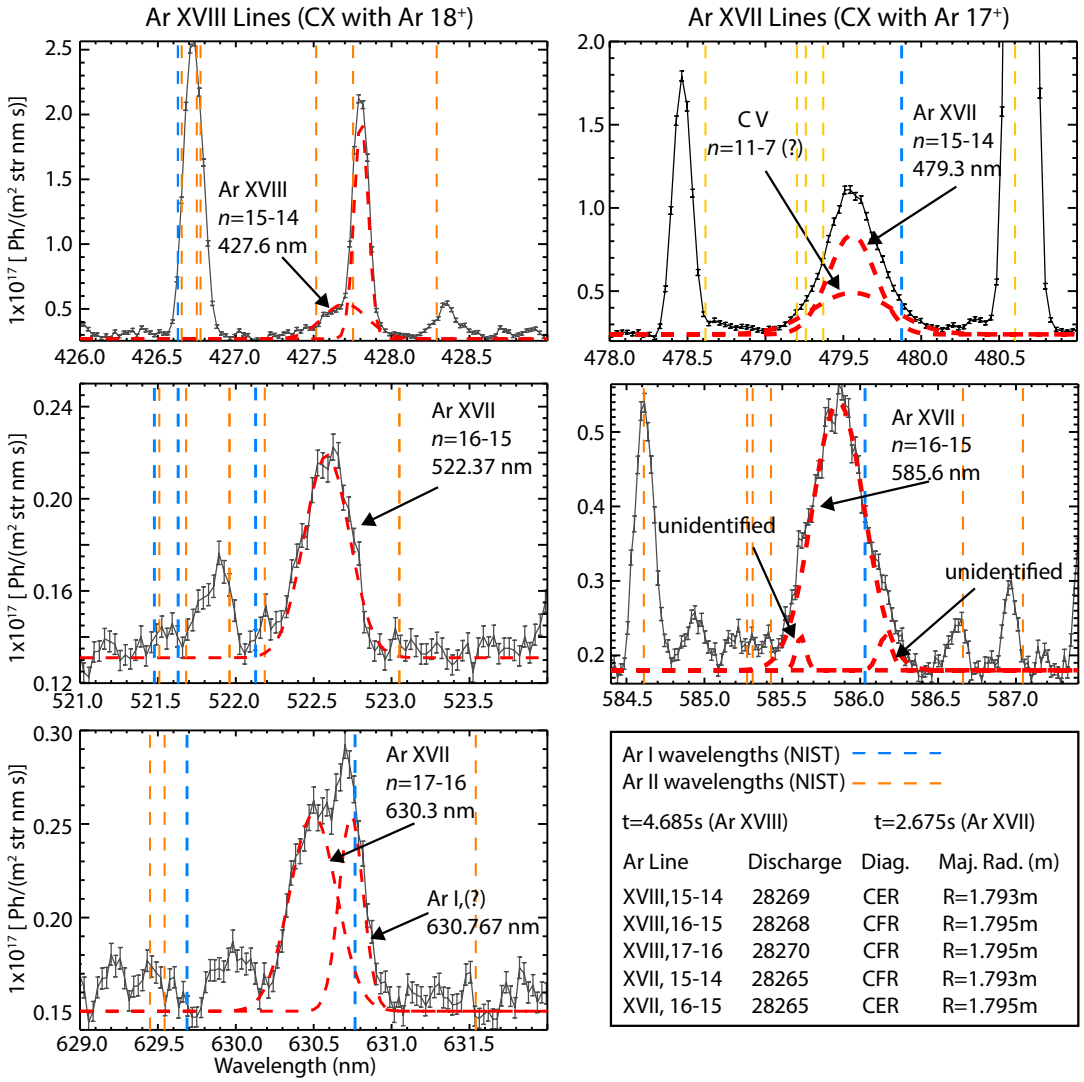

Figure 1. Example spectra corresponding to charge exchange with Ar 18^+(left) and Ar 17^+ (right). In addition, the wavelength positions of Ar I and Ar II lines taken from the NIST spectral line database are shown as blue and orange dashed vertical lines, respectively. The red dashed lines show the Gaussian components of the fits to the spectra. All spectra were obtained in very similar discharges and the spectra are absolutely calibrated with the exception of the Ar XVII n=15-14 line at 479.30 nm measured on the CFR spectrometer. This system does not have an absolute calibration at this wavelength. Here, a scaling factor was applied such that the Bremsstrahlung background at this wavelength matched that measured at 586 nm in the same discharge along a similar LOS accounting for the $1/\lambda$ dependence.

region that shows a clear radial dependence in width, shift, and intensity consistent with a low-Z CX emission line, very likely the C V n=11-7 transition emitting at ∼479.7 nm. This is further supported by the good agreement achieved between the electron and ion temperature profiles when the C line (in the absence of Ar puffing) is fitted using an atomic mass of 10-12 amu. Unfortunately, no other ion temperature measurements are available in this discharge for comparison. The presence of a second charge exchange line of similar intensity in the same wavelength region complicates the interpretation. It is very difficult to unambiguously separate the contributions from these two lines without additional constraints on the fitting. However, it is not straightforward to constrain the lines to the same temperature and rotation as the Zeeman and fine structure splitting are very different for the two impurity species. A much more complicated fitting of this spectra would be necessary to reliably extract the Ar emission for further analysis and interpretation. The Ar XVII n=16-15 line (middle panel, right hand column of Fig. 1) does not suffer from this problem. However, it is also not ideal due to presence of many small emission lines in the background and beneath the spectra. As will be discussed in the next section, the interpretation of Ar CX spectra is already sufficiently complicated that, if possible, all perturbations to the spectra should be avoided.

For the Ar^{+16} population, three lines have been examined. Example spectra are shown in Fig. 2. For the Ar XVI n=14-13 transition, the line emission is quite low compared to near-by spectral lines and the number of counts measured on the CCD systems is lower than for the transitions at higher wavelength. However, the line can still be cleanly identified and reasonable profiles produced. This line was also used in [1]. The n=15-14 transition shown in the middle panel of Fig. 2 is the principle line used at AUG for Ar investigations and the line used for the majority of the work shown in this publication. This emission line has only one disadvantage, namely, that the He I n=7-4 emission is also at this wavelength. If there is He in the plasma, even at relatively low concentrations, this emission can complicate the fit to the data. This will be discussed further in the next section. The third Ar XVI emission line overlaps with the wings of the D_α spectrum at 662.2 nm, see the bottom panel of Fig. 2. If the slope in the background is accounted for, this line can also provide information on the Ar^{+16} charge state. However, it significantly increases the difficulty in properly accounting for the fine structure splitting and additional steps must be taken to block the D_α emission. Either a wire or filter must be included in the spectrometer design or the cold D_α emission must be shifted off of the CCD camera to avoid saturation, as was done in the example shown here.

2.1. Zeeman and fine structure corrections

In order to extract temperatures from the measured argon spectra, the apparent widths must be corrected for the Zeeman and fine structure (FS) broadening of the spectral lines. In addition, the fine structure also impacts the fitted position of the lines, necessitating corrections to the apparent rotation. The Zeeman splitting, being

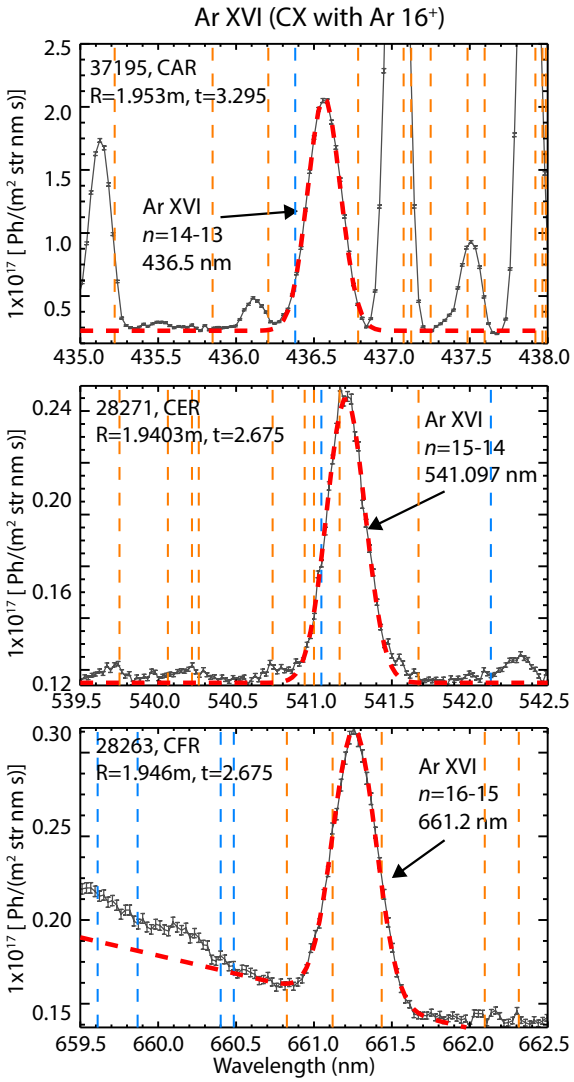

Figure 2. Example spectra of helium-like Ar CX emission lines. In addition, the wavelength positions of Ar I and Ar II lines taken from the NIST spectral line database are shown as blue and orange dashed vertical lines, respectively. The red dashed lines show the Gaussian components of the fits to the spectra. The n=15-16 and n=16-15 spectra were measured in very similar plasmas to those used for the measurements of the Ar XVIII and XVII lines shown in Fig. 1. The n =14-13 transition was measured in piggyback in a completely different set of experiments, hence its intensity can not be directed compared to those of the other measured Ar lines.

symmetric, does not impact the rotation measurement.

In order to take these effects into account the full splitting patterns were calculated for a grid of true ion temperatures between 50 eV and 20 keV, magnetic fields between 0 T and 5 T, and angles of observation between 0 and 90 degrees. Then, as a first attempt, these spectra were all fit with a single Gaussian and the fitted widths and positions used to determine the relationship between true and apparent temperature and rotation. The rest wavelengths of the lines were determined by calculating the center of mass (COM)

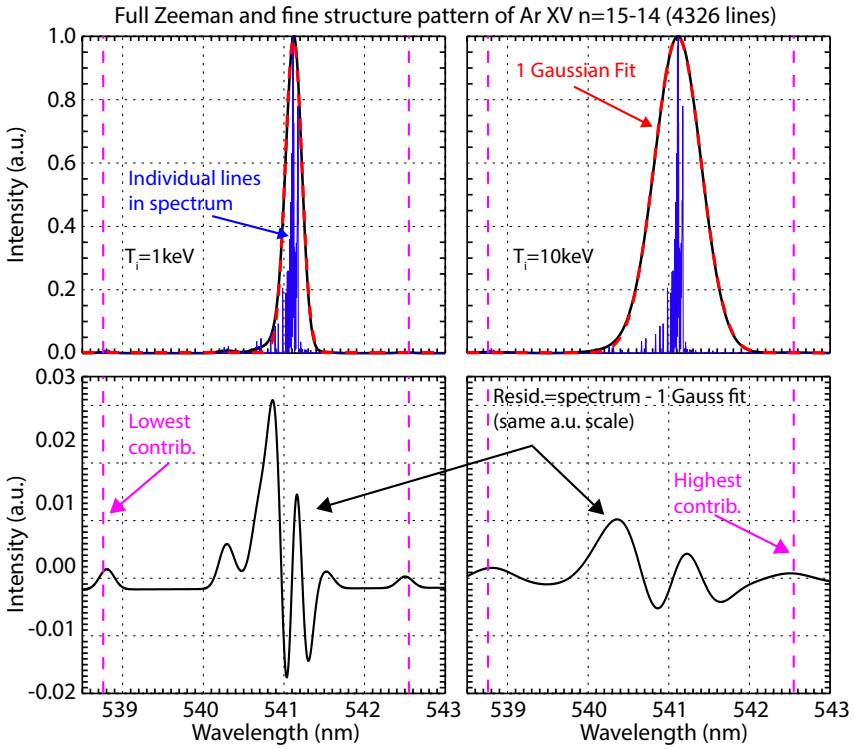

Figure 3. (Top) Calculated Zeeman and fine structure splitting pattern for the Ar XVI n=15-14 transition at 541.0997 nm for an ion temperature of 1 keV (left) and 10 keV (right). The individual lines contributing to the spectra are shown in blue while the total line shape is given in black. Single Gaussian fits to the spectra are also shown in red. The magenta lines indicate the lowest and highest wavelength lines that contribute to the spectra. In the bottom row the residuals of the Gaussian fit to the total spectrum are shown.

of the entire distribution. These central wavelengths are given in Table 1. Examples of the full calculated pattern (blue) and resultant line shapes (black) are shown in the top row of Fig. 3 for the Ar XVI n=15-14 transition at true ion temperatures of 1 keV (left) and 10 keV (right). These patterns were calculated for a magnetic field of 2 T and a 0.1 degree angle to the magnetic field. In contrast to low-Z line emission, the resultant line shapes are non-Gaussian even at high ion temperatures (10 keV). Single Gaussian fits to the spectra are shown as red dashed lines and the residuals of the fits are shown in the bottom panels. The fine structure splitting of the line results in an effective 'tail' on the low-wavelength side of the line. As a result single Gaussian fits to the spectra always result in fitted-positions that are higher than the COM of the line and, therefore, rotations that are too high.

In addition, there are contributions to the total spectrum that are ∼1.5 nm above and below the COM of the distribution. The positions of the highest and lowest wavelength contributions are indicated in Fig. 3 by dashed magenta lines. These high- and low-wavelength contributions do not significantly influence the Gaussian fitted positions of the line in these simulations or in the experiment, but they do contribute

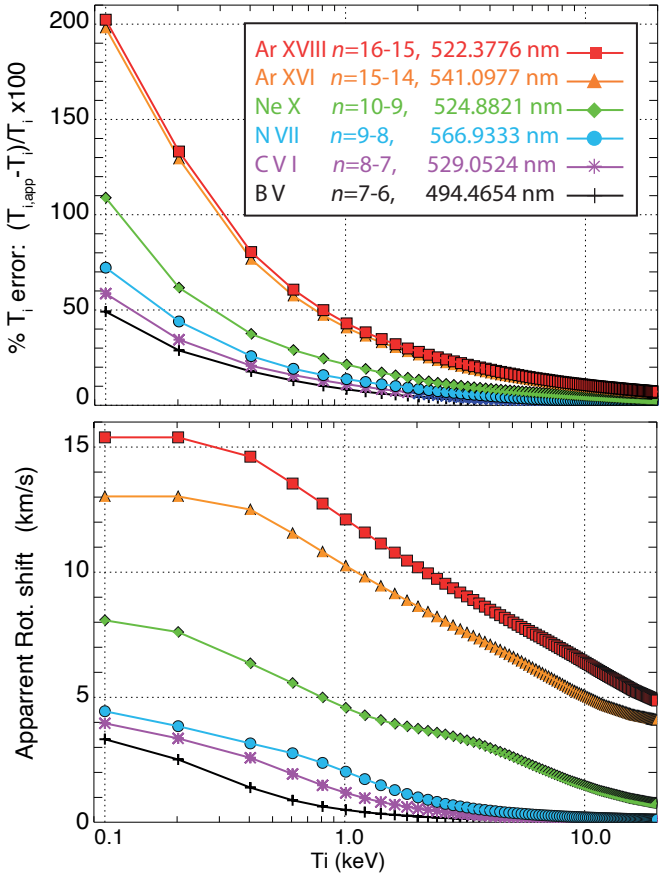

Figure 4. (Top) Percent error between the apparent and true ion temperature due to the Zeeman and fine structure splitting of the spectral line for a variety of CX emission lines and (Bottom) apparent shift in rotation due to fine structure splitting of the spectral line both as a function of true ion temperature. These are calculated for a magnetic field of 2T and an angle to the field of 0.1 degrees. The wavelength given per transition is the COM of the Zeeman and fine structure splitting pattern.

to the calculated rest-wavelength, and hence the corrections that must be applied to produce correct rotations. These lines also are partially responsible for the fact that even at $T_i \sim 20$ keV, the fitted position of the line does not approach the rest wavelength as determined by the COM of the distribution. Rather, temperatures of several hundred keV are required before these outlying contributions are fully enfolded in the Doppler broadening of a single Gaussian fit. In Fig. 4, the correction curves for the ion temperature and toroidal rotation are shown as a function of true ion temperature for the same field and observation angle as in Fig. 2.1. The ion temperature corrections are shown as percent of the true ion temperature while the rotation correction is shown as the shift away from the COM of the distribution in km/s. Here, one sees that the correction to the Ar ion temperature doesn't drop to the 10% level until almost 10 keV and the rotation corrections, shown in the bottom panel, can be as high as 15 km/s at low T_i and remain above 5 km/s for typical core ion temperatures (T_i <10 keV) at AUG.

For comparison the corresponding corrections for the standard boron, carbon, nitrogen, and neon charge exchange lines are also given. These curves clearly show the scaling with the charge, Z. The ion temperature corrections, while smaller for these impurities, are not negligible at low T_i. Similarly, the correction to the rotation can also be quite important. However, one should note that the application of the rotation corrections depends on what value is used for the rest wavelength in the fitting of the experimental spectra. The curves shown here use the COM of the full Zeeman and FS patterns as the rest wavelengths. These values are given in the legend of Fig. 4. However, if a different rest wavelength is used in the fitting, as is often the case, the corresponding curve can be shifted up or down accordingly to provide the appropriate rotation correction.

At AUG corrections for the Zeeman broadening and fine structure broadening and shift are routinely applied to the measured data for all CX lines ($Z \leq 10$) via the single Gaussian approximation described above. This is done after the measured spectra have been fitted to a single Gaussian convolved with the instrument function of the system to extract the apparent temperature and rotation and, therefore, requires that the temperature of the instrument function is small compared to the apparent width of the line. This condition is easily satisfied for all of the lower-Z impurities and also for the Ar measurements investigated here. At AUG the core systems regularly used to measure argon [14, 15] have instrument functions on the order of 0.08nm, which (for mass=39 amu) contribute a broadening of roughly 150 eV to the spectra, enabling pedestal top temperatures of 400-500 eV to be resolved. However, most Ar^{+16} measurements are made in regions of the plasma with ion temperatures of 1 keV or higher. For Ar CXRS measurements, the same approach was taken for correcting the apparent temperatures and rotations. However, as will be shown, this simplified assumption is insufficient to reliably produce the correct ion temperatures to better than a few hundred eV or rotations to better than $\sim$ 10 km/s.

Dedicated experiments were performed to validate the available argon CX cross-sections. These experiments will be described in detail in section 4. Here, it important only to note that they took place on a day when the He concentration in AUG was not negligibly small. As such, the He II n=7-4 emission, which exists in the same wavelength range as the Ar XVI n=15-14 transition, can not a priori be neglected in the analysis. In the discharges of interest here, no CX He measurements were available on account of the He CXRS system having been used to measure boron to provide reference ion temperature and rotation profiles. In addition, the standard CXRS He transition (He II n=4-3) is disturbed by argon seeding and can not reliably be used during Ar puffing. However, information on the He population via the n=4-3 CX line is available in the pulses both before and after the discharges of interest, and were at similar plasma currents and NBI heating powers. These discharges show edge He CXRS intensities (including plume) on the order of 1-2% of the electron density.

An examination of the measured spectra before the first Ar puff (see Fig. 8) in discharge 37052 clearly show the presence of the He n=7-4 CX line. This is shown in

the top left panel of Fig. 5 for one edge radial channel at 2.945s. Here, the active plus plume emission is 7x10^{16} ph/(m^2-str-s) while the passive emission is 3x10^{16} ph/(m^2-str-s). These emissions, while small, are also not entirely negligible compared to the relatively low Ar intensities measured in these experiments. Fig. 11 in Section 5 shows the measured Ar^{+16} intensity profiles measured at the peak of the second Ar puff.

As the He emission can not be ignored in these plasmas, several different methods have been employed to isolate the Ar emission from the total measured spectra. First, the He spectra measured in a 50 ms time window just before the first Ar puff have been used as a background measurement and subtracted equally from all subsequent spectra in the discharge. However, at AUG the He content in the plasma is often observed to decay during a plasma discharge, suggesting that the He emission subtracted from the Ar spectra might be too large for later time points. While no measurement of the core He content exists in this pulse, SOL He lines are observed by the SPRED VUV spectrometer [16], and these demonstrate a mild decay over the course of the plasma discharge. Therefore, for comparison, a second set of data was produced in which the He spectra from before the Ar puff were scaled in time to match the time evolution of the SPRED measurement and these were subtracted from the total spectra to isolate the Ar intensity. Finally, a third method was employed in which the Ar spectra were fit to a total of three Gaussians: two Gaussians to model the He components and the third to capture the Ar. This third method, however, was eventually deemed unsatisfactory as, even with strong constraints on the fitted widths and positions of the He lines, their intensities invariably acquired a similar temporal behavior to the Ar, particularly at the edge, indicating that the three components were not well separated. All three methods, however, yielded Ar intensity profiles that were extremely similar inside of ρ_ϕ =0.75 to within 5% percent. For comparison, neglecting the He contributions altogether yields intensities that are higher by up to 30%. Therefore, the Ar impurity density analysis presented in section 5 is relatively robust to the method used, so long as the He has, in some way, been taken into account. That analysis uses Ar intensities obtained via the first method, namely a simple subtraction of the He spectra measured prior to the first Ar puff. The analysis of the ion temperature and toroidal rotation are significantly more sensitive.

An example of a measured Ar XVI n=15-14 spectrum, obtained by the simple subtraction method, is shown in the bottom left panel of Fig. 5 together with a single Gaussian fit and the instrument function of the system. In addition, in the residuals the fine structure asymmetry can just be seen outside of the noise on the spectrum, although, in this case, it can't be ruled out that the He subtraction process has not influenced the asymmetry. However, spectra from other discharges without He contamination show similarly shaped spectral lines. Here, one can also see the increase in the Bremsstrahlung emission from before to during the Ar puff by comparing the background level in the two spectra shown on the left hand side. In the next section, this increase in Bremsstrahlung will be used to deduce the change in Z_{eff} due to the Ar puff. In the right hand panels the corrected (black) and non-corrected (red) argon temperatures and rotations are shown

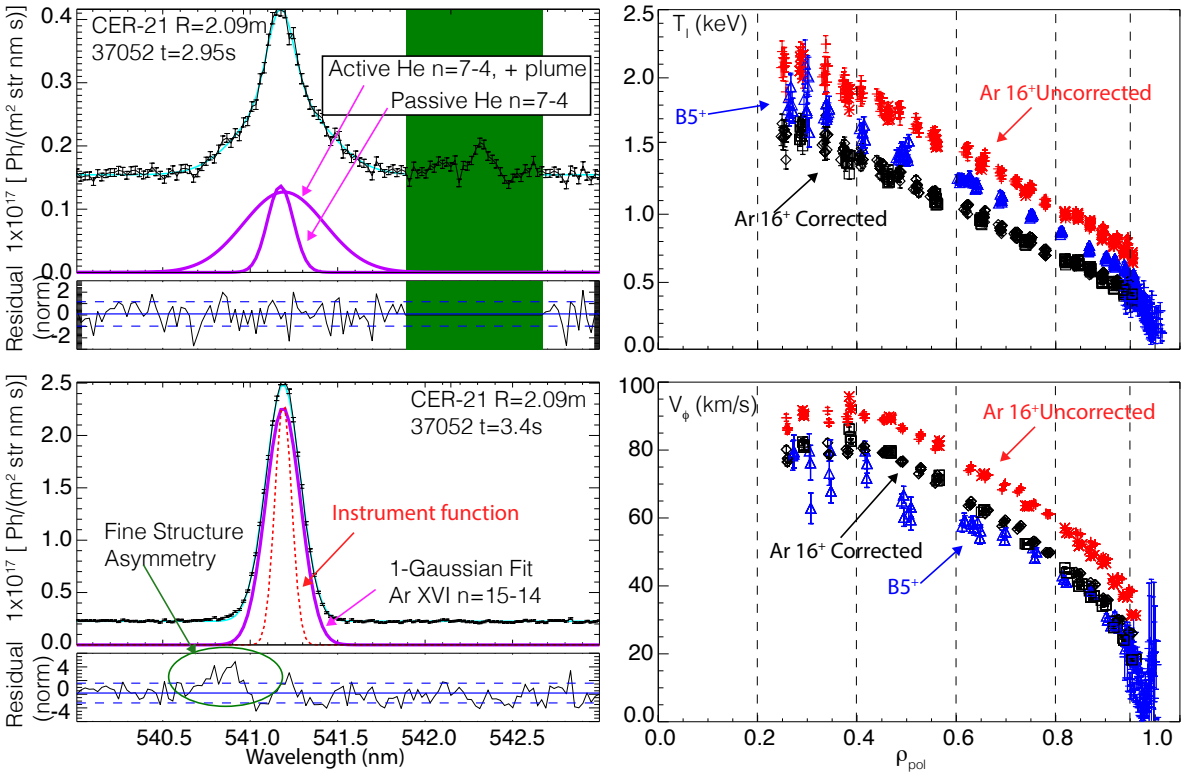

Figure 5. (Left) He n=7-4 spectra measured prior to first Ar puff in discharge 37052 and an Ar XVI n=15-14 spectrum measured in the second Ar puff with the He spectrum subtracted. (Right) Ion temperature and rotation profiles from the fits to the Ar with (black diamonds) and without (red crosses) corrections for Zeeman and fine structure. The profiles obtained from CXRS with B 5^+ are also shown (blue triangles).

together with the profiles measured from CXRS with B^{+5} n=7-6. The uncorrected argon temperatures and rotations are significantly higher than those obtained from boron as expected. The boron profiles have also been corrected for Zeeman splitting and fine structure, but in this case the corrections are minimal and the uncorrected profiles are not shown for the sake of clarity. With the 1-Gaussian fit corrections described above, the Ar temperatures are too low, while the rotation is reasonably well recovered.

In this case, the discrepancy in the corrected temperatures and rotations could conceivably be due to the impact of He on the spectra, if the measures taken to remove it were insufficient or over-compensated. However, the discrepancy is quite reproducible for all phases of the Ar puffs and for all of the methods tested. In addition, a further examination of over thirty discharges, many of which do not suffer from He contamination, with cross-comparisons to boron, carbon, and nitrogen CXRS profiles shows that this over-correction of the ion temperature is quite robust, while the rotation is reasonably, albeit not perfectly, reproduced. This observation motivated a reexamination of the methodology for determining the Zeeman and fine structure corrections to the Ar spectra. The problem lies in the asymmetry of the Ar spectra. In the calculated splitting patterns the asymmetry is clearly and *maximally* present

(see Fig. 3) and, therefore, exerts a *maximum* influence on the single Gaussian fits to the theoretical spectrum resulting in *maximum* correction curves. In the experiment, however, the fine structure asymmetry is obscured and its impact reduced due to the presence of a Bremsstrahlung background, photon noise, the readout noise of the cameras, and potentially other contributions to the measured spectra, such as the He emission.

To at least partially mimic this, the theoretical Ar spectra were refit as a function of true ion temperature, magnetic field, angle to the magnetic field, and signal to background with flat backgrounds being added to the spectra. In all cases Poisson weighting ($1/y$) was used in the least-squares fit to the data. This naturally results in sets of correction curves that are smaller than those shown in Fig. 4, giving improved agreement with the profiles measured on other impurities. However, also with these corrections, quantitative agreement is not achieved in all cases. The best agreement in ion temperature has been obtained by creating correction curves from 2-Gaussian fits to the theoretical spectra, one to account for the main Ar emission, and a second to account for the fine-structure asymmetry on the low wavelength side of the line. This is done with fixed constraints on the relative heights, positions, and widths of the Gaussians, and the same model is then applied to the experimental spectra. This method generally gives good agreement in ion temperature, but often creates a shift in rotation, unless the fine structure asymmetry is particularly clear in the experimental data.

To date, the authors have not found a unique set of correction curves that can be applied together with a simple fit recipe that reliably reproduce accurate temperature and rotation profiles for all cases. However, the developed recipes generally can reproduce correct ion temperatures to within ~ 100 eV and rotations to better than 10 km/s. Further development of Ar fitting techniques, for example, fitting to the complete Zeeman and fine structure split pattern is left for future development. It should be noted that in all cases, while the subtleties on the shape of the spectra and the fitting method have a non-negligible impact on the derived temperatures and rotations, the resulting intensity profiles are quite robust. Therefore, provided validated CX cross-sections, impurity densities can be derived from simple fits to the Ar spectra.

3. Available Ar charge exchange cross-sections

Although the intensity profile of the emission, L_{CX}, for a given impurity, Z, and transition, λ, can be obtained directly and simply from the fits to the spectra, the translation of this information to impurity density, n_z is not straightforward. The impurity density is proportional to L_{CX}, but also depends on the effective emission rates, $\langle \sigma v \rangle$, for charge exchange with neutral atoms with quantum number n and energy j, and the integral of the neutral density, n_0, along the line of sight (LOS), direction 's'. If n_Z is constant along the LOS, it can be solved for via equation 2.

$$n_Z = \frac{4\pi}{h\nu} \frac{L_{CX,z}(\lambda)}{\sum_n \sum_j \langle \sigma_{n,j,Z,\lambda} v_j \rangle_{\text{eff}} \int_{LOS} n_{0,n,j}(s)\, ds}. \tag{2}$$

The methods used at AUG to calculate the neutral densities and evaluate equation 2 are discussed in detail in [10]. This work also demonstrates the importance of the n=2 halo population to the CXRS analysis. To obtain accurate CXRS densities for low-Z impurities, not only the beam-impact CXRS cross-sections must be known, but also the probability of charge exchange between thermal impurities and thermal neutrals in the n=2. Moreover, the importance of the n=2 halo population to the CX measurement increased with "Z" for the impurities considered in that work (He-Ne). Therefore, for argon CX, this population can not a priori be neglected.

The accuracy of the CXRS impurity density analysis relies on the accuracy of the cross-section data. In the case of argon, several different sets of argon charge exchange cross-sections exist and these vary widely in both absolute magnitude and energy dependence. The standard ADAS package [17, 18], for example, contains n and l resolved charge exchange cross section data for n=1 atomic hydrogen colliding with Ar^{+16}, Ar^{+17}, and Ar^{+18} from both the ORNL calculations [1] as well as from the 'Universal Formula' (UF) [19]. The ADAS files corresponding to these data are: qcx#h0_ornl#ar16.dat, qcx#h0_ornl#ar17.dat, and qcx#h0_ornl#ar18.dat for the ORNL datasets and ext#h0_arf07#ar16.dat, ext#h0_arf07#ar17.dat, and ext#h0_arf07l#ar18.dat for the UF.

The ORNL cross-sections were determined from classical trajectory Monte Caro (CTMC) calculations performed at Oak Ridge National Laboratories (ORNL) and are the same as were utilized in Whyte *et al* [1]. The ORNL datasets available through OPEN-ADAS [18] do not include collisions with H in the n=2. These calculations were extended in [2] making the data more comprehensive and validated via fully quantum mechanical calculations. In this work calculations for charge exchange with H in the n=2 are included, but not at the thermal energies needed to include halo contributions to the CXRS signal. In Fig. 6 the cross-section data for charge exchange between H and Ar^{+16} into the n=15 are shown for all available datasets as a function of interaction energy. The ORNL dataset available in OPEN-ADAS is shown as black diamonds while the newer calculations published in Schultz *et al* [2] are shown as magenta triangles. The n=1 data from the two sources are effectively identical. Therefore, in this work, only the ORNL data is included in the comparisons shown in section 5.

The data from the OPEN-ADAS UF file for collisions with H in the n=1 is also shown as hollow blue squares. This dataset is several orders of magnitude larger than the ORNL data set at the energies relevant for CXRS measurements at AUG, which are indicated by dashed orange lines. This is because the scaling laws used here [19] to calculate charge exchange cross-sections for arbitrary Z and n and to extrapolate to higher Z rely on the Ar calculations of Errea *et al* [3], shown as red circles and discussed below. The cross-sections provided by the UF can only be as good as the datasets used to produce the scaling laws. Therefore, this dataset is also not used in the comparisons shown in section 5. It is included here only for the sake of completeness. Of more interest are the n=2 cross-sections produced by the formula (OPEN-ADAS: ext#h0_arf07#ar16_n2.dat, ext#h0_arf07#ar17_n2.dat,

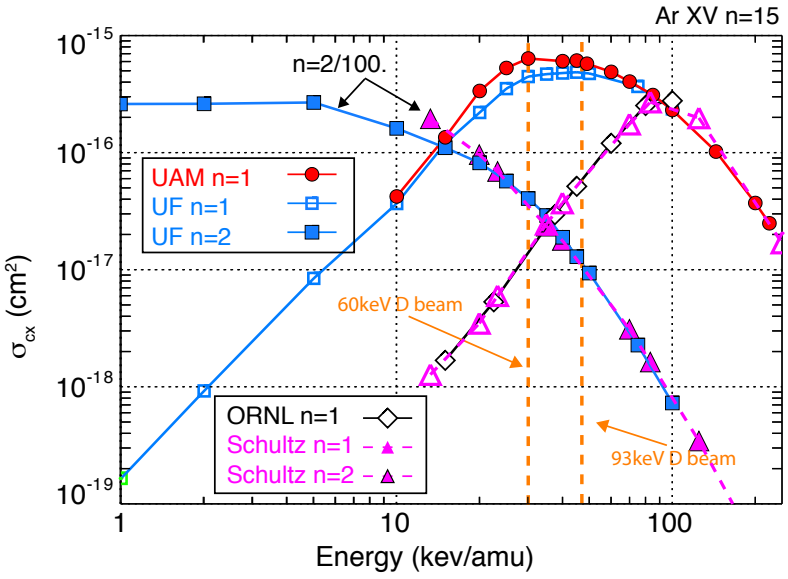

Figure 6. Charge exchange cross-sections into the n = 15 for collisions between H (n=1,2) and Ar^{+16}. The n=2 cross-sections have been divided by 100 to compare them more easily to the n=1 datasets.

ext#h0_arf07#ar18_n2.dat,). These are shown as blue, fillled squares and have been divided by a factor of 100 for easier comparison. The UF calculations have the advantage that they can be performed for any impact energy, hence these n=2 cross-sections are also available at thermal energies and for the calculation of effective rates presented below, these n=2 cross-sections have been re-calculated over a finer grid at low energies. It in interesting to note that these cross-sections agree well with the n=2 data from Schultz *et al* [2] in the energy region in which they overlap. The reliability of UF n=2 data is additionally examined in section 5.

The final set of argon charge exchange cross-sections shown in Fig. 6 was produced by and is available through the Universidad Autonóma in Madrid (UAM) [3]. These files are not available via OPEN-ADAS except for collisions between H in the n=1 and Ar 18^+ (qcx#h0_uam#ar18.dat). The UAM calculations differ from the ORNL dataset primarily in that they use a hydrogenic distribution to describe the capture into high n-shells. The ORNL CTMC calculations used a single micro-canonical distribution to describe the initial state. Guzman *et al* [20] show that CTMC calculations of CX cross-sections to high n are more accurate if a collection of microcanonical initial distributions, known as an hydrogenic initial distribution, is used to describe the initial target and donor electron distributions in the coordinate space. This allows a more appropriate treatment of the wave-functions of high n's, which are more extended in the coordinate space. The caveat is a loss of precision of the initial electron distribution in momentum space, which the microcanonical distribution describes exactly. That is an intrinsic limitation of Monte Carlo calculations [21]. Errea *et al* show that at collision energies less than 100 keV/amu these two different assumptions lead to order of magnitude

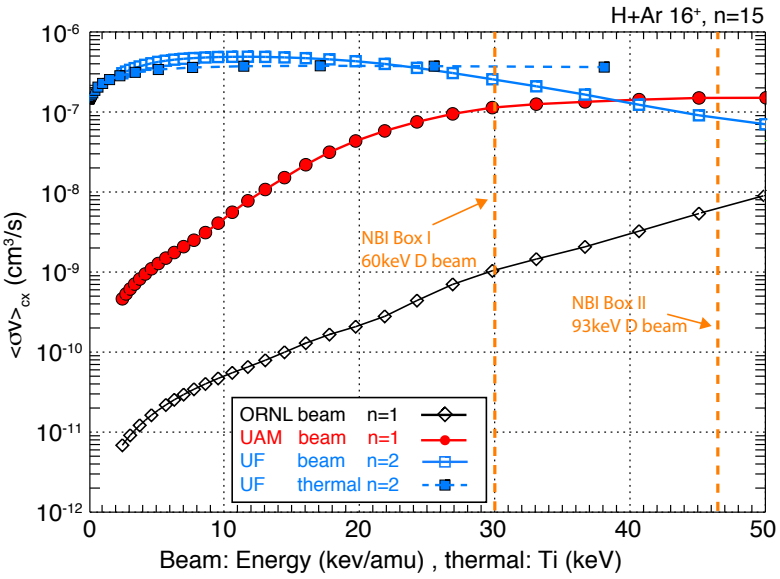

Figure 7. Effective emission rates for CX reactions between Ar^{+16} and H neutrals calculated from the cross-section data shown in Fig. 6 . These were calculated for an electron density of 5.6x10^{19} m^{-3}, an ion temperature of 2300 eV, and Z_{eff}=1. The abscissa here is beam energy per atomic mass unit (amu) for the case of beam-impact effective rates and the ion temperature for the thermal $n = 2$ cross-sections shown (blue squares + dashed line). Note that the effective emission rates have only been calculated for the range of impact energies that are seen in the experiment. (<50 keV/amu).

differences in the calculated cross-sections at relevant neutral beam energies. This can be seen in Fig. 6. Cross-sections for CX with H in the n=2 are not available in the UAM datasets.

From the cross-section data, effective emission rates can be calculated. This was done for the ORNL and UAM n=1 datasets as well as the UF n=2 cross-section data identically via the procedure described in [10]. In Fig. 7 the effective emission rates calculated from the cross-section data shown in Fig. 6 are shown for an electron density of n_e=5.6x10^{19} m^{-3}, an ion temperature of 2300 eV, and Z_{eff}=1. Here it should be noted that cascade from higher n-states into the n=state of interest, while included in these calculations has only been considered up to n=20. For the high-n transitions of interest for Ar CX, this might not be sufficient to fully describe the relevant population [12]. As such, these effective emission rates likely underestimate the true photon emission rates that correspond to their respective cross-section datasets.

From Fig. 7 it is clear that the two sets of effective emission rates will result in very different argon densities. The use of the ORNL data will lead to much higher Ar densities than the UAM dataset. Moreover, the energy dependences are significantly different. The results of Schlummer *et al* [13] indicate that for CX with Ar 17^+ the CTMC approach of Schultz *et al* [2] is more accurate than that of Errea *et al* [3]. This work utilized x-ray measurements of CX into lower n states than considered here. For the high

n state transitions needed to make Ar CXRS measurements in the visible, the work of Guzman *et al* suggests that the UAM cross-sections should be more appropriate. In the following sections, both the absolute magnitude as well as the energy dependence of the beam-impact charge exchange cross-sections between H and Ar^{+16} focusing on the n=15-14 transition will be tested. This is done experimentally by making CXRS measurements at different beam energies, evaluating the impurity densities using the different available n=1 effective rates, and comparing the results to the soft-x-ray measurements and Z_{eff} from Bremsstrahlung diagnostics.

The inclusion of the n=2 halo contribution must be neglected in this initial comparison. However, information on the n=2 cross-sections can be gleaned indirectly, by checking if the inclusion of the n=2 halo contribution improves the agreement between the datasets collected at different neutral beam injection energies. If the energy dependence of the beam-impact cross-sections is correct, then it must be possible to bring the CX measurements at different beam energies into agreement through the use of a single n=2 cross-section value. If this is not possible, it indicates an incorrect energy dependence. The experiments designed for these purposes and their results are presented in Section 4.

4. Experiment description and data analysis

AUG is equipped with two neutral beam injection (NBI) boxes with four NBI sources per box. Each source injects 2.5 MW of power in D operation, but the extraction voltage differs between the boxes. NBI I operates with a full acceleration voltage of 60 keV in D, while NBI II operates with 93 keV. In addition, AUG has dedicated CXRS diagnostics viewing neutral beam sources in both NBI Box I and II. The 'CER' diagnostic is focused on source 3 in NBI box I [14], while the 'COR' diagnostic views source 8 of NBI box II [15]. When these two NBI sources are in use, it is possible to make simultaneous measurements of impurity profiles using two different energy beams. This provides an automatic test of the energy dependence of the charge exchange cross-sections, as both calculations must yield the same impurity density profiles. Moreover, on a discharge-to-discharge basis, it is possible to reduce the voltage on both NBI boxes.

In the experiments presented here, the acceleration voltage of NBI Box I was reduced from 60 to 50 keV and the voltage of NBI Box II from 93 to 70 keV, providing a four-point scan in the energy dependence of the CXRS cross-sections performed over two consecutive AUG discharges, 37052 and 37053. Time traces of important plasma and machine parameters from these discharges are shown in Fig. 8. These discharges were lower-single-null, type-I ELMy H-mode, deuterium plasmas, with a plasma current of 1.0 MA, a magnetic field of -2.5 T, low shaping (δ_{ave}=022 and κ=1.67), and a confinement factor of $H_{98} \sim 0.83$. The discharges were heated with a combination of NBI and electron cyclotron resonance heating (ECRH), which at AUG is commonly used to prevent tungsten accumulation. Time traces of the heating powers for these discharges can be seen in the top panels of Fig. 8. Here the total NBI powers for

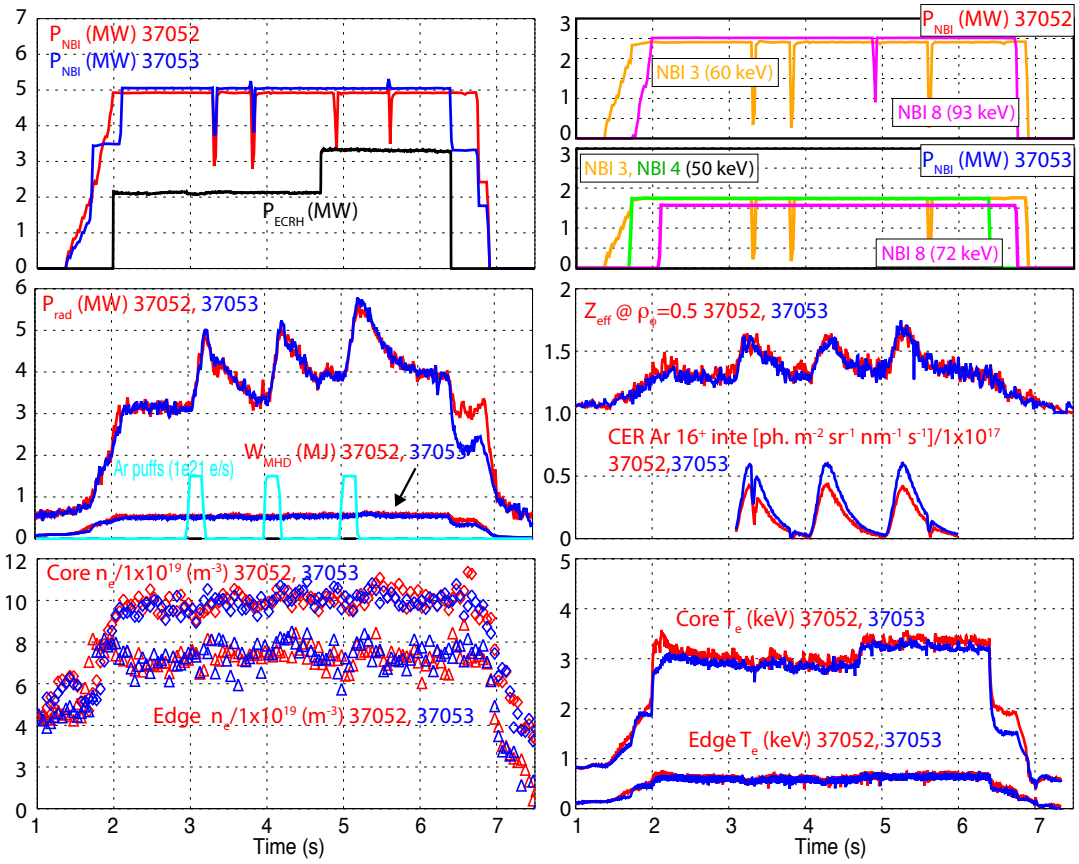

Figure 8. Time traces of important plasma and machine parameters for AUG discharges 37052 and 37053.

the two discharges are shown in the top left panel, while the powers delivered by the individual beams sources are shown in the top right. The CXRS beams, NBI 3 and 8, are used in both discharges. In discharge 37053 the beam voltages were reduced for the beam energy scan. This results in reduced injected power, hence an additional NBI source, NBI 4, was included to keep the total power constant. In the top left panel also the injected ECRH power is shown. This time trace corresponds to 37052, but the ECRH power was identical in 37053.

The stored energy, radiated power, and injected Ar puffs are shown in the middle, left-hand panel. Here, one can see that the discharges are very comparable, and that the Ar slowly accumulates during the discharge, causing an increase in the total radiated power, but remains less than the total injected heating power (top left). The middle-right panel shows the value of Z_{eff} determined from Bremsstrahlung radiation [22] at mid-radius together with the intensity of the Ar^{+16} CXRS line from the CER diagnostic at the same location. Note that the radiated power and Z_{eff} values at the beginning of discharge 37053 reproduce those of 37052 very well, indicating that there is very little residual Ar present in the plasma from the previous discharge.

The intensities of the Ar^{+16} emission measured by the CXRS diagnostics are not

the same in the two discharges. This is the result of several effects. First, there is the change in the charge exchange cross-sections when the beam voltage is reduced. Second, when the beam voltage is reduced, the beam current is as well to keep the beams operating on their perveance curves. And, lastly, for the CER diagnostic, these two effects are compensated by the fact that in 37053 NBI 4 was also used to keep the total applied NBI power the same. The lines of sight (LOS) of the CER intersect both beams, and hence also gather CX signal from this source, which has to be included in the modeling. In the bottom panels of Fig. 8 the core and edge electron densities (left) and temperatures (right) are shown. Here too, one can see that the discharges are very reproducible and neither shows significant changes in density or temperature during the Ar puffs.

In order to test the different sets of CXRS cross-section data, it is necessary to know the Ar^{+16} density in the plasma. For this purpose, the best calibrated measurement available is the visual Bremsstrahung (VB) measured as background along the LOS of all CXRS diagnostics. This analysis has the advantage that it is based on absolutely calibrated diagnostics that are re-calibrated before and after every experimental campaign. These discharges took place very early in the 2020 experimental campaign before any degradation of the diagnostics is likely to have occurred. A 10-20% degradation over the course of a campaign is normal for this wavelength region. This conjecture is supported by the excellent agreement in impurity densities and Z_{eff} produced by the CER and the COR diagnostics at this time. Typically, the COR diagnostic degrades before the CER on account of its optical components being situated in the torus, while the CER optics are external. Therefore, the absolute calibration of the line-integrated visual Bremsstrahlung measurement is estimated at 10% and this non-Gaussian uncertainty has been added to, and in fact dominates, the error estimates on the fits to the Bremsstrahlung background. The fits were performed using a $1/\lambda$ dependence, both photon and read-out noise are included in the error bars included in the fits, and care was taken to remove spectral line emissions.

The change in Bremsstrahlung emission along the LOS is shown in the left hand panel of Fig. 9 for three LOS of the CER diagnostic. The shaded regions represent the measured VB while the symbols correspond to the model as discussed below. The LOS intersect the plasma toroidally and have tangency radii of ρ_{pol} ~0.2, 0.6, and 0.8. Similar measurements are available along, in total, 48 LOS with different, albeit all toroidal, paths through the plasma. Together, these measurements place fairly strong constraints on the absolute magnitude of Ar that can be present in the plasma and give clear indications on the shape of the Ar density profile.

The contribution of a given species to the measured VB integrated along the LOS at a given wavelength λ (alternatively, frequency ν) is

$$B_{LOS}(\lambda) = \int 6.1285\times10^{-18} n_e n_z Z^2 (T_e)^{-1/2} e^{-h\nu/T_e} g_f(T_e, Z, \nu)\, \lambda S(\lambda)\, dl. \quad (3)$$

Here, the electron temperature, T_e is in eV, the densities are in m^{-3}, the Gaunt factors are taken from Sutherland *et al* [23], and the function $S(\lambda)$ is spectrometer specific and

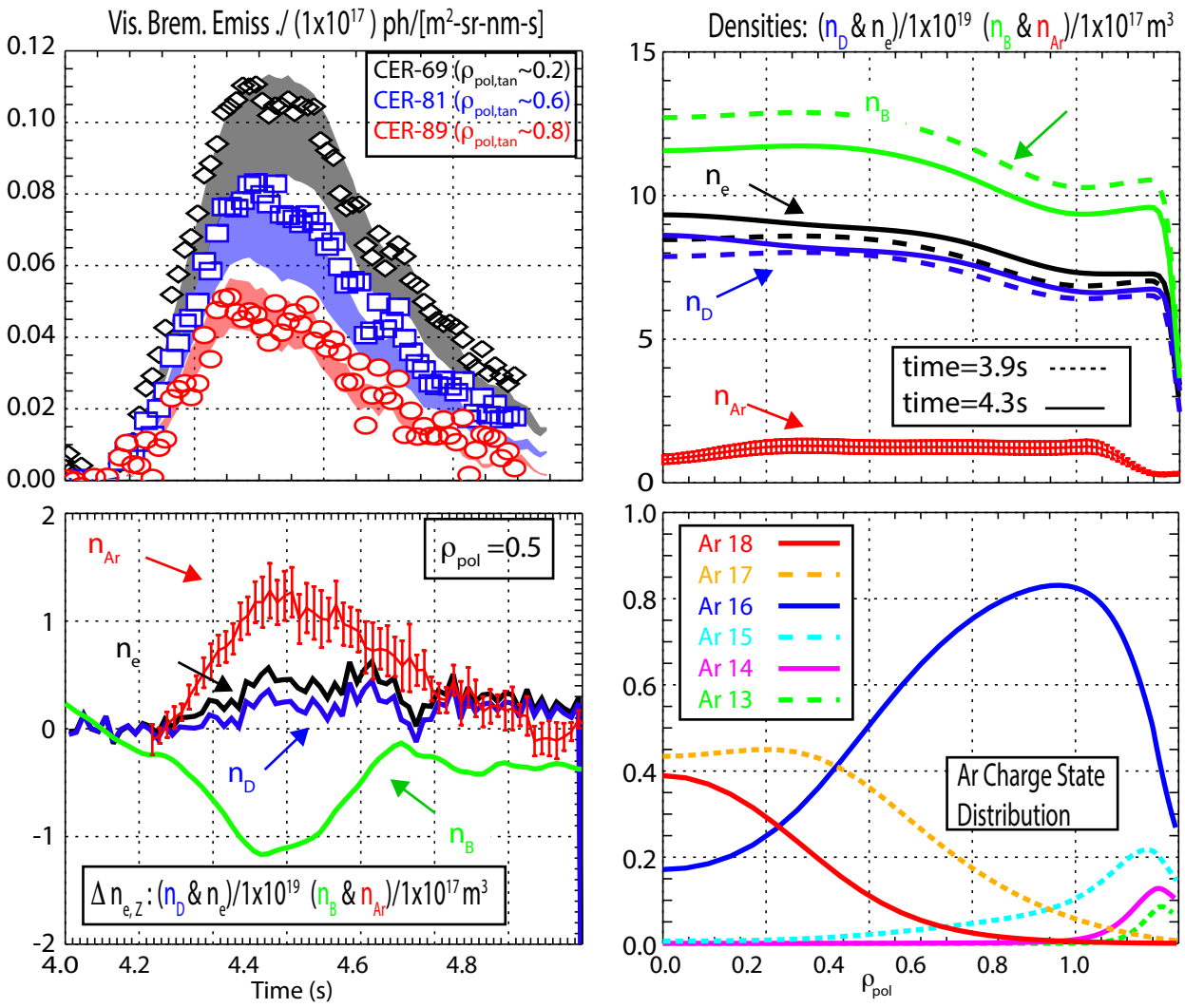

Figure 9. (Top left) Measured (shaded region) and modeled (symbols) changes in the VB measured during the second Ar puff in discharge 37052. (Top right) Electron, deuterium, effective boron, and total argon density profiles. (Bottom left) The corresponding time evolutions of the density profiles at mid-radius. The boron density (green) is effective in the sense that it represents the total low-Z impurity contributions to Z_{eff} before the Ar puff and is coupled with the measured time evolution of the boron population. (Bottom right) Normalized distribution of the argon charge states calculated using STRAHL and the n_e and T_e profiles averaged over the time window 4.25-4.35s.

gives the photon energy incident on a given pixel in eV/nm. The measured changes in the LOS integrated VB along all of the LOS have been modeled using a simple assumption on the shape of the total argon density profile, and the measured electron density and temperature profiles. An effective low-Z impurity density profile with a charge of 5 (B) designed to match the measured Z_{eff} value before the Ar puff is also included. This profile is then given the time history of the measured boron density, which is observed to decrease by 10% during the Ar puff, see bottom left panel of Fig. 9. The deuterium profiles used are self-consistent with the measured electron density, the low-Z impurity density behavior, and the modeled Ar populations. The STRAHL code has been used to calculate the argon charge state distribution, this is shown in the bottom right panel of Fig. 9. Ar populations between 15^+ and 18^+ are included in the model of the VB.

For each LOS the measured VB at each time point is balanced against the contributions from D, B, and the four Ar populations to solve for the constant 'C' in the Ar density profile, Eq. 4.

$$n_{Ar,Tot} = Cf\left(\rho_{pol}\right), \tag{4}$$

To start, it is assumed that the entire change in the VB is due to the addition of Ar. This, however, results in too high Ar densities, as it does not take into account the change in the deuterium contribution to the VB, which is dominant even at the peak of the argon puff and sensitive to both changes in the electron density and impurity densities. Therefore, the Ar and D densities are self-consistently iterated until the produced VB converges to the measured value. This is done for all LOS and for every time point. The shape of the assumed total argon density ($f\left(\rho_{pol}\right)$) is then adjusted until the same 'C' is obtained, within error bars, for each LOS. In order to reproduce the VB measured along all LOS, a decrease in the total Ar density profile towards the plasma edge is required as well as a hollow region in the plasma center. The final shaped used in these calculations can be seen in the top right panel of Fig. 9. The shape of the total Ar density profile is assumed to be constant during the entire Ar puff.

The total modeled VB integrated along the same three diagnostic LOS are shown as symbols in the top left hand panel of Fig. 9. The electron, deuterium, total argon, and effective boron density profiles are shown in the top right panel for two time points: before the Ar puff in dashed lines and at the time point of maximum Ar density in the plasma in solid lines. The corresponding time histories at mid-radius are shown in the bottom left panel. This analysis assumes that all low-Z impurities behave similarly to the measured B impurity. However, the low-Z impurities make very little difference to the change in the measured VB or to the change in the deuterium densities and an error in this population would not significantly change the results. The error bars shown on the Ar densities contain only two sources of error: the error on the measured VB and the variation of the factor "C" from the different LOS, as, although they converge well, are not identical due to errors on the assumed shape of the argon profile as well as the error on the density profile and time history. The Ar^{+14} population has not been

included, making the total argon density profile shape outside of ρ_{pol} =0.8 incorrect. In addition, the charge state distribution from STRAHL in this region is incorrect due to the neglect of CX with thermal deuterium [16]. As such, all quantitative comparisons of the Ar^{+16} densities focus on smaller plasma radii.

The argon densities derived via this procedure can also be compared to those derived from the Z_{eff} integrated data analysis of the same data [22]. In this case, however, the derived argon densities are too low by 20%, on account of the Gaunt factors. The Z_{eff} analysis assumes that the Gaunt factors are similar for all contributing species and can be represented by the Gaunt factor associated with the effective charge. However, the Gaunt factor for Ar and other higher Z impurities is different from D and low-Z impurities by 20% or more, depending on the electron temperature, and causes the changes in Z_{eff} in the presence of higher-Z impurity puffing to be too small. The changes in Z_{eff} shown in Fig. 8 suffer from this error. However, when the change in Z_{eff} is analyzed via the present method, but using the incorrect Gaunt factors (Z_{eff} dependent), the results of the IDZ analysis are reproduced, demonstrating the consistency of the two independent analyses.

Information on the argon density in the plasma is also available via the soft X-ray diagnostics. The suite of soft x-ray diagnostics comprises several hundred LOS, enabling full tomographic inversions of this data [24, 25]. Time traces and radial profiles of the flux-surface-averaged (FSA) soft X-ray emissivity are shown in the top row of Fig. 10. These correspond to the second Ar puff in discharge 37052. Here, the time window 3.9-4.0 s was used as a 'background' measurement: the emissivity in this phase was subtracted from the soft X-ray data to isolate the emission due to a single Ar puff only. The error bars shown on the experimental data indicate the statistical uncertainty of the inversion only. They do not include any systematic or calibration errors.

In addition to the experimental data, the results of modeling the Ar density in the plasma with STRAHL are shown as highlighted curves. Here, the transport of Ar in the scrape-off-layer (SOL) and confined plasma region was optimized such that both the temporal and radial behavior of the soft X-ray Ar measurements are well reproduced. To obtain a good temporal match between the STRAHL-modeled Ar behavior and the experiment, a delay of 60 ms was introduced into the STRAHL time base. The authors speculate that this 60 ms corresponds to the transit-time of the argon from the valve into the SOL. It might also suggest that the role of wall recycling is not sufficiently well modeled. The profiles of diffusion (D) and convection (V) used are shown in the bottom left panel. These were kept constant in time. Strong decreases in the transport coefficients in the edge pedestal were needed to reproduce the fast rise of the Ar in the plasma. The soft X-ray is best reproduced with a small inward pinch in the edge, though considerable variation is possible while still reaching reasonable agreement with the data. In the plasma core the STRAHL simulation over-predicts the soft X-ray, which is hollow consistent with the VB data, and suggests the presence of a region of outward convection, likely linked to the presence of sawteeth in these discharges. Quantitative comparisons of argon densities are, therefore, restricted to the region 0.3

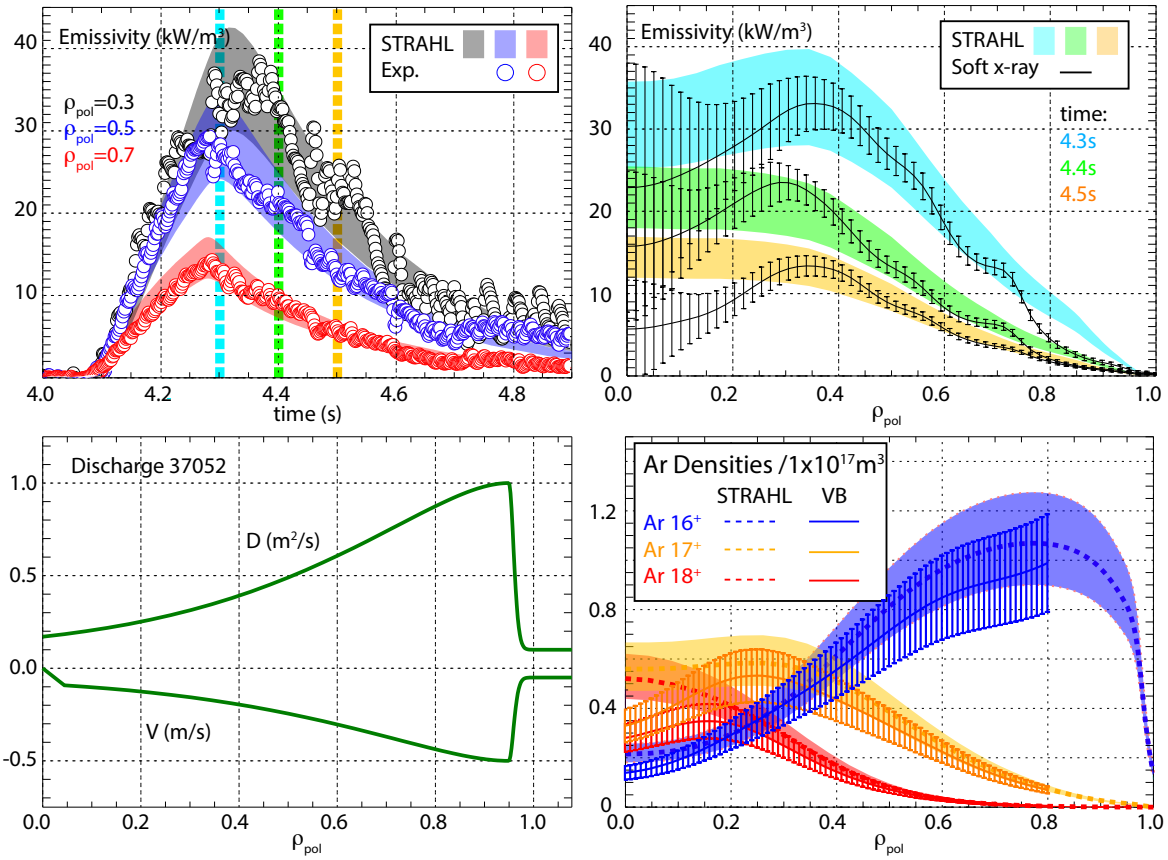

Figure 10. (Top) Measured and modeled flux-surface-averaged soft X-ray emissivities as a function of time (left) at three different radial positions and as a function of ρ_{pol} (right) at three different time points in the second Ar puff of discharge 37052. The time points for which the radial profiles are shown are highlighted in corresponding colors in the time-trace plot. (Bottom) Profiles of diffusion and convection used in the STRAHL modeling (left) and the Ar density profiles from the STRAHL modeling (solid lines) as well as the result of the VB analysis.

$< \rho_{pol} <$0.8. The authors do not claim that the combination of D and V shown here is the most optimized solution, other combinations might well improve the modeling. However, validation of argon transport is not the aim of this study, and this solution is sufficient to determine how much Ar must be present in the plasma to reproduce the observed soft X-ray emissivities. The 'uncertainty' bands on the STRAHL curves were created by varying the source rate of the modeled Ar puff until the modeled emissivity bands reasonably encompassed the error bars on the measured emissivity data. This is admittedly not a rigorous procedure, and these bands can not be thought of as Gaussian error bars. However, they do effectively demonstrate the range of Ar densities that would produce soft x-ray emissivities within the statistical error bars of the experimental soft x-ray deconvolution.

The STRAHL modeled argon densities are shown in the bottom right hand panel for the Ar^{+16}, Ar^{+17}, and Ar^{+18} charge states. The result from the VB analysis are also

shown. These two calculations agree very well, indeed within 10% and certainly within the uncertainties of the respective analyses.

5. Impurity Density Analysis from CXRS Ar Intensities

The CXRS intensity profiles measured by the CER and CUR diagnostics at 4.3s in discharges 37052 and 37053 are shown in the left top panel of Fig. 11. Here, the 50 keV (black circles) and 60 keV (blue diamonds) intensity profiles were measured by the CER diagnostic on NBI 3 (60keV, discharge 37052) and on a combination of NBI 3 and 4 (50 keV, discharge 37053). The measured intensity is larger for the 50 keV case even though the beam current was reduced together with the beam voltage, because of the use of two sources from that neutral beam box. See equation 2 for the relationship between measured CX intensity and the local neutral density populations. On the right hand side the line integrated neutral densities for the first energy component in the ground state and the n=2 halo are shown. The neutral densities of the second and third beam energy components are not shown as, for almost all cases, these components contribute only on the 10% level or less to the total CXRS signal. This can be seen in the bottom left panel where the percent contribution to the total CXRS signal considering only beam impact CX with the ground state populations is shown. For neutral beam energies of 50 and 60 keV the first energy component dominates the signal. At 70 and 92 keV, however, the second energy component can start to be important if the UAM cross-sections are taken. In addition to the first energy n=1 population, the neutral densities for the n=2 halo population are also shown in the bottom right panel, as these are expected to contribute non-negligibly to the CXRS signal.

Both neutral density populations are higher for the 50 keV case than they are for the 60 keV case, consistent with the observed difference in the measured intensities for those two energies. It is also interesting to note that the 60 keV and 92 keV cases show very similar measured intensities together with very different neutral densities. Even taking into account the increasing importance of the second beam energy component at increasing beam energies, very different CX cross-sections are needed to obtain the same impurity density from these two measurements. Finally, the densities of the n=2 halo are lowest for the 70 and 93 keV beams and, more importantly, the halo densities are very similar in these two cases. Therefore, the neglect of the n=2 halo can't explain any observed differences in the argon densities from these two beam energies, making these two datasets ideal targets for testing the energy dependence of the available cross-section data.

The Ar density profiles obtained from the measured intensities are shown in Fig. 12 for both the ORNL (top) and UAM (bottom) cross-section data. The left hand panels show radial profiles averaged over the time window 4.25 to 4.35s, while the right hand panels show time histories at $\rho_{pol} = 0.55$ for a single Ar puff. These densities only include contributions from beam impact charge exchange with neutrals in the n=1. The impurity densities calculated with the ORNL dataset are too large by a

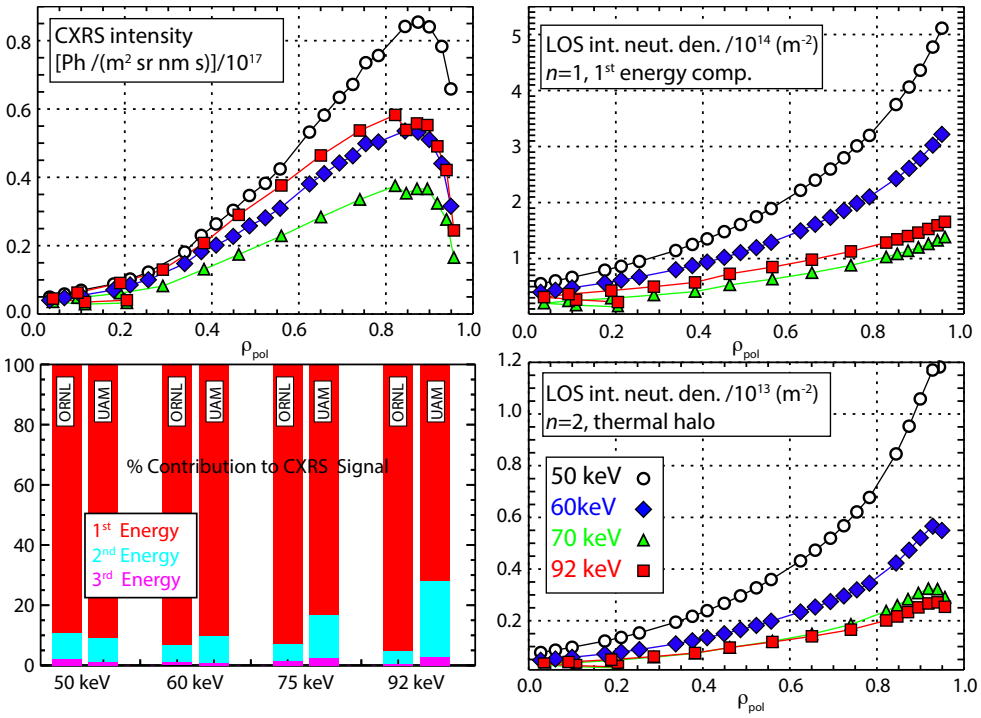

Figure 11. (Top left) Ar^{+16} CXRS intensities (Ar XVI n=15-14) in discharges 37052 and 37053 measured on neutral beams with four different injection energies. (Right) Line integrated (along CXRS diagnostic LOS) neutral density of the first energy component in the ground state (top right) and of the n=2 population of the thermal halo (Bottom Right). The percent contribution to the total CXRS signal only taking into account n=1 beam impact CXRS is shown in the bottom left.

factor of 10-50 (cross-sections too small) depending on the beam energy when compared to the Ar densities derived from the change in VB. The extreme differences observed between the different energy components (factor of 5) clearly demonstrate that the energy dependence is much too steep. The differences in the n=2 halo densities for the four different cases can not remedy these differences. In particular, the discrepancy seen between the 70 and 92 keV cases, which feature very similar neutral halo density populations, can not be resolved by the addition of an n=2 contribution.

The densities derived from the UAM atomic data, on the other hand, are a factor of 2-2.5 below the Ar^{+16} density from VB, indicating that these rates are too large. However, they do a significantly better job at producing consistent impurity density profiles at the different beam energies. The error bars shown on these profiles (ORNL and UAM) are constructed from the measured error bars on the CXRS intensity profiles, which are very small, and a fixed 10% assumption on the calculated neutral density profiles, which dominates the error bar shown here. In addition, it is generally assumed that there is an additional 10% on the absolute intensity calibration of the diagnostics. This has not been included, as the relative calibration of the diagnostics is more important for determining the energy dependence. These experiments were performed very early in the 2020 experimental campaign and the excellent agreement

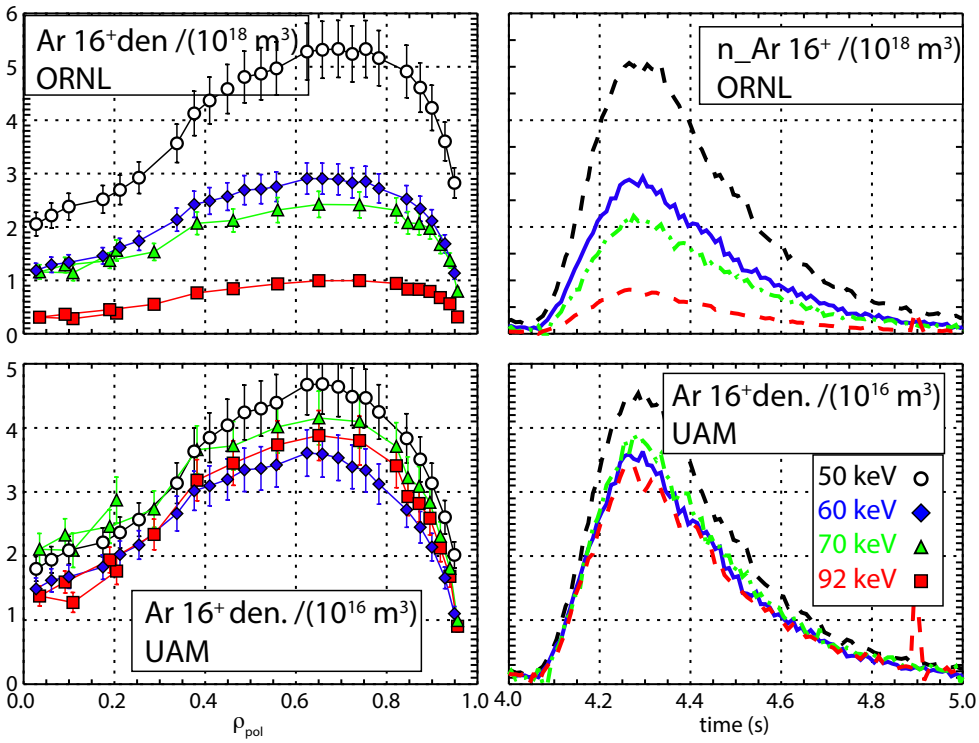

Figure 12. Ar^{+16} CXRS density profiles (left) and time traces (right) calculated using ORNL cross-sections (top) and UAM cross-sectinos (bottom). These profiles include only beam impact CX with the neutrals in the n=1.

between the impurity densities (B/C/N) and the Z_{eff} from these diagnostics indicates that the relative intensity calibration error is less than 10%.

While the impurity densities calculated for the different beam energies using the UAM cross-sections mostly agree quite well, the 50 and 60 keV sets still differ outside of uncertainties with the 50 keV data too high and the 60 keV data too low compared to the 70 and 93 keV profiles. The n=2 halo density population is largest for the 50 keV beam, indicating that the inclusion of this population will help to improve the agreement. However, as the 60 keV dataset is already below the 75 and 92 keV cases, the inclusion of n=2 cannot be expected to fully remedy the situation.

The UAM n=1 effective rates best reproduce the VB Ar^{+16} densities when they are scaled downward by a factor of 2.32. This is shown in the top left hand panel of Fig. 13. Here, the CXRS profiles made on the 50 and 60 keV beams (diagnostic on NBI box I) have been interpolated onto the radial base of the NBI box II system (70 and 92 keV measurements) to facilitate the comparison between the diagnostics. In the top right hand panel, one can also see the result of including the n=2 effective rates from the Universal Formula in the calculation. The inclusion of an additional neutral population, for a fixed measured intensity, reduces the total impurity density resulting from the calculation, see Eqn. 2. This is why the scaling factor on the n=1 cross-sections increases from 2.32 to 2.7. The n=1 and n=2 rates were allowed to vary, down in the case

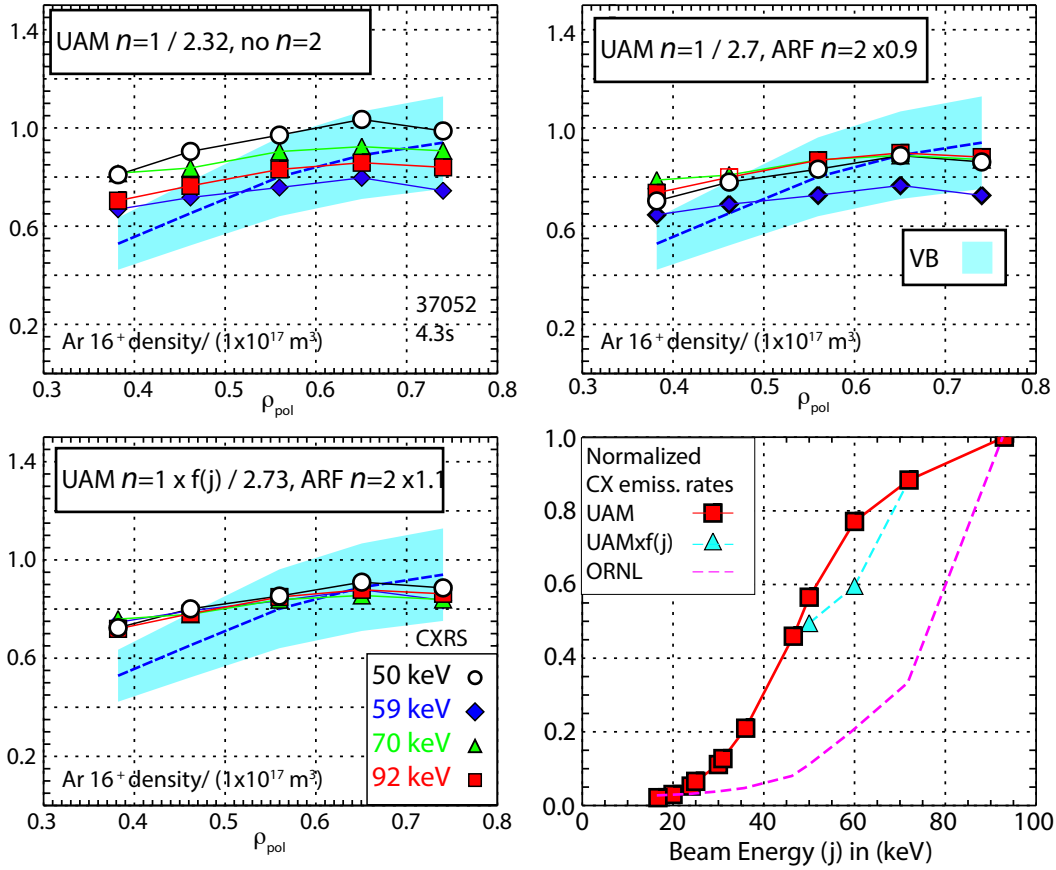

Figure 13. (Left and top right panels) CXRS Ar^{+16} density profiles made on four different energy beams calculated with a variety of modifications to the UAM n=1 effective rates and with and without the inclusion of the n=2 rates from the universal formula. (Bottom right) Energy dependences of the UAM (red squares), UF (red diamonds), and ORNL (dashed magenta line) effective rates for the density and temperatures at mid-radius, at 4.3s in discharge 37052. In addition, modifications to the UAM and ARF datasets that provide the best matches to the experimental data (cyan triangles and circles) are shown.

of the n=1 and up and down in the case of the $n = 2$, to find the combination that best reproduces the Ar^{+16} densities from VB and minimizes the variance between the four primary beam energies. Interestingly, the best combination is found with only a 10% change to the Universal Formula n=2 effective rates. When the n=1 rates are forced to be further away from the optimum solution, significantly larger n=2 rates are required to compensate and result in significantly larger variations between the datasets. The fact that the optimum solution is found with n=2 effective rates so near the original UF dataset and with overall Ar 16^+ densities so near the VB values is an excellent demonstration of the consistency of the various datasets involved in this analysis.

The inclusion of the n=2 halo population improves the agreement of the four datasets. In this case, the 50 keV dataset is brought into reasonable agreement with the 70 and 92 keV data, at the expense of the 60 keV data, which sits 15% below. There are several possible explanations for this behavior. First, there could be an error

on the measured intensity profile for the 60 keV case. However, the spectra and fits have been checked and the intensity profile is quite robust as discussed earlier in this work. Second, an error in the absolute calibration could impact the comparison, but this would effect the 50 keV intensity profile as well, as they were measured with the same system. This possibility can not bring the 60 keV dataset into agreement with the others, without shifting the problem to the 50 keV dataset. Moreover, the intensity calibrations for these diagnostics also enter into the Z_{eff} measurements derived from the Bremsstrahlung background and provide excellent agreement on both discharges, further indicating that this is not a diagnostic issue. A second possibility is a problem with the neutral density calculations on this discharge. However, these calculations have been checked and compared to the neutral densities obtained in other discharges in which B or N, were measured on both diagnostic systems (60 and 90 keV beams). The neutral densities are very comparable between these discharges and in the case of B and N CX measurements result in the same impurity density profile regardless of which beam energy or beam combination is used. Therefore, it is unlikely that the neutral density calculation is at fault, though this can be a source of increased error.

The last and most likely possibility is that the energy dependence of the UAM cross-sections at intermediate energies (50-70 keV) is too shallow. A steeper energy dependence, would enable the experimental measurements made on all beam energies to be brought into better agreement. To find the change needed to bring the four datasets into best agreement, the energy dependence of the UAM effective rates was systematically reduced between 45 and 70 keV and the best solution for the energy dependence, as well as the overall scaling of the n=1 and n=2, found. The change needed to the energy dependence is shown in the bottom right panel of Fig. 13: the difference between the red squares and the cyan triangles. The resultant CXRS density profiles using this solution are shown in the bottom left hand panel. The overall scaling factor on the n=1 is effectively unchanged and, again, the best solution is found within 10% (this time an increase) of the original UF n=2 data. It should be noted that while this combination of energy dependence, n=1 and n=2 effective rates reproduce the experimental data very well, it is not a unique solution. It is certainly possible to produce multiple variations on this theme. However, they all will tend towards a reduction of the cross-section in the region around 60 keV, resulting in a slightly steeper energy dependence.

In conclusion, the results of the CXRS analysis show that the 'ORNL' cross-sections for beam impact CX with Ar^{+16} calculated in [1, 2, 13], are an order of magnitude too small and can not reproduce the energy dependence seen in the experiment. The UAM data [3], on the other hand, is a factor of 2.73 too big, but does a significantly better job of reproducing the energy dependence seen in the experiment. Still, 15% changes to the energy dependence of this dataset are required to bring the Ar density profiles measured on different energy beams into agreement, and this is only possible with the inclusion of the n=2 halo population. Moreover, the variation between the different energy CXRS datasets is best minimized when using a scale factor on the n=1 UAM

data that reproduces the VB (and soft x-ray) Ar densities and only 10% modifications on the UF n=2 rates, demonstrating a surprising degree of consistency between the different elements of the analysis.

For an accurate assessment of Ar^{+16} densities from CXRS measurements on the Ar XVI n=15-14 transition at 541.09773 nm the authors recommend to use the UAM effective rates scaled downward by a factor of 2.73 and the UF n=2 scaled upward by 1.1. In addition, the authors recommend a reduction of the energy dependence of the cross-sections around 60 keV by, for lack of more detailed data, the simple linear function $f(j)$ given in Table 2. Even with these corrections, the authors estimate the overall uncertainty on the magnitude of the resultant densities to be at least ± 20%, as it was not possible to quantify the argon density present in the plasma via soft x-ray or VB measurements to better than this, and within this range of Ar densities, it easily possible to find alternative solutions for the n=1 and n=2 scale factors and $f(j)$.

Energy (keV)	f (j))
0.	1.0
45.	1.0
50.	0.88
60.	0.77
70.	1.0
100.	1.0

Table 2. Linear corrections to be applied to the energy dependence of the UAM n=1 effective rates to produce consistent Ar^{+16} density profiles from the Ar XVI n=15-14 transition. This correction is to be applied in addition to the overall factor of 2.73. Energies below 45 keV and above 70 keV are not affected by this correction.

6. Discussion

Argon is being considered as a pedestal and diverter radiator for future fusion devices. Experiments in present day devices are necessary to assess the effectiveness of Ar as a divertor and mantle radiator, to study its transport and its impact on core plasma confinement, as well as its compatibility with other key aspects of tokamak operation such as pedestal stability and ELM mitigation scenarios. For these experiments, it would be extremely useful to have accurate measurements of the Ar densities in the confined plasma region. At AUG, such information is available via changes in the visual Bremsstrahlung and via the soft x-ray data. However, neither of these methods can uniquely isolate the Ar contribution to their respective intensities in the presence of other non-constant impurity density profiles, such as tungsten accumulation or changes in impurity profiles due to transport. CXRS measurements of the Ar density profiles

are, therefore, of great interest. With CXRS, local, time-resolved, argon density profiles could be provided irrespective of the behavior of other impurities in the plasma.

To this end, eight different visible charge exchange lines with three different charge states of Ar have been explored to identify the best charge exchange lines to use in present day experiments. For typical AUG plasma parameters Ar^{+16} is the charge state of the most interest, as it typically exists over the widest range of plasma radii compared to Ar^{+15}, Ar^{+17}, or Ar^{+18}. For CX with Ar^{+16}, the ArXV n=15-14 was identified as the best transition. For CX with Ar the apparent broadening due to the Zeeman effect and broadening and shift to the fine structure is larger than for lower-Z impurities and must be taken into account in the interpretation of the measured Ar spectra to obtain accurate ion temperature and rotation profiles. Not taking these effects into account can lead to incorrect ion temperature and rotation measurements of several hundred eV and up to 15 km/s, respectively, when measuring on Ar. Unfortunately, due the large asymmetries associated with the fine structure, correction curves can not be straightforwardly applied with simple one or two Gaussian models as has been done for lower-Z impurities. Rather, detailed modeling of the complete pattern, most likely convolved with the instrument function of the system will be required to produce reliable temperature and rotation profiles.

For the evaluation of Ar density profiles accurate charge exchange cross-sections are required. There are two main sets of cross-section data available for CX with Ar^{+16}: the data calculated at ORNL [1, 2] and by UAM [3]. For Ar^{+16}, these cross-sections differ by over an order of magnitude at the beam energies of interest and have very different interaction energy dependences. In this work, CXRS measurements were made on four different energy beams between 50 and 92 keV and both sets of cross-sections were used to calculate the resulting Ar density profiles. These densities were then compared to the argon densities derived from the measured changes in the visual Bremsstrahlung and soft x-ray emissivities, which were in very good agreement.

The Ar density profiles calculated using the ORNL datasets are 10-50$\times$ too large while the UAM Ar densities were a factor of 2.73 too small. The UAM dataset did a much better job at capturing the energy dependence. Using the UAM dataset and considering only beam impact CX, the Ar density profiles made on the four different energy beams differed by only 25% and the inclusion of n=2 halo contributions improved this agreement to within 15%. This agreement could be further improved by subtle changes to the energy dependence of the n=1 cross-sections. If the energy dependence were slightly steeper around 60 keV then the Ar density profiles from all four beam energies would agree to better than 10%. With these corrections in place, the fudge factor of 2.73 brings the Ar^{+16} densities from CX into excellent agreement with the soft x-ray and VB measurements.

From the work presented here, the authors conclude that the CTMC calculations of Errea *et al*, which use a hydrogenic distribution to describe the initial target and donor distributions better reproduce the experimental data. This initial assumption, in contrast to the single micro-canonical distribution used in Schultz *et al*, increases

the charge exchange cross-sections at the relevant beam energies to the correct order of magnitude (too high by a factor of 2.73) and enables the observed energy dependence to be mostly recovered. This is true, at least, for CX with Ar^{+16} when looking at the high n transitions in the visible. This is not in disagreement with the work of Schlummer *et al*, which examined CX with Ar^{+17} into lower n than we consider here and concluded the opposite, as a single micro-canonical distribution is expected to describe the lower n transitions better. This work does demonstrate that further experimental validation of argon cross-sections is required as well as additional development in the calculation of higher-Z, high-n charge exchange cross-sections. The extension of the experiments performed here to higher charge states of Ar and other transitions is the subject of future work.

Acknowledgments

The authors would like to acknowledge and thank D. Schultz for his useful explanations, for making the charge exchange cross-section datasets from [2] and [13] available, and his openness to collaboration. The authors would also like to thank T. Odstrcil for his assistance with the tomographic inversions of the soft X-ray data used in this work as well as his very useful insights and suggestions. In addition, F. Guzman acknowledges support from the NSF (AST-1816537), and NASA (ATP 17-0141). This work has been carried out within the framework of the EUROfusion Consortium and has received funding from the Euratom research and training programme 2014-2018 and 2019-2020 under grant agreement No 633053. The views and opinions expressed herein do not necessarily reflect those of the European Commission.

[1] D. G. Whyte *et al*. Phys. Plasmas., 5:3694, 1998.
[2] D. Schultz*et al*. J. Phys. B At. Mol. Opt. Phys, 43:144002, 2010.
[3] L. F. Errea*et al*. J. Phys. B At. Mol. Opt. Phys, 39:L91, 2006.
[4] G. Pacher *et al*. Nucl. Fusion, 47:469, 2007.
[5] K. Tobita *et al*. Nucl. Fusion, 49:075029, 2009.
[6] A. Kallenbach *et al*. J. Nucl. Matter, 415:AS19, 2011.
[7] A. Kallenbach *et al*. Plasma Phys. Control. Fusion, 55:124041, 2013.
[8] A. Kallenbach *et al*. Nucl. Fusion, in press https://doi.org/10.1088/1741-4326/abbba0, 2020.
[9] R. C. Isler *et al*. Nucl. Fusion, 24:1559, 1984.
[10] R. M. McDermott *et al*. Plasma Phys. Control. Fusion, 60:095007, 2018.
[11] S. T. A. Kumar *et al*. Plasma Phys. Control. Fusion, 54:012002, 2012.
[12] H.P. Summers*et al*. Plasma Phys. Control. Fusion, 48:263, 2006.
[13] T. Schlummer *et al*. J. Phys. B At. Mol. Opt. Phys, 48:144033, 2015.
[14] E. Viezzer *et al*. Rev. Sci. Instrum., 83:103501, 2012.
[15] R. M. McDermott *et al*. Rev. Sci. Instrum., 88:073508, 2017.
[16] R. Dux *et al*. Nucl. Fusion, in press https://doi.org/10.1088/1741-4326/abb748, 2020.
[17] H.P. Summers. ADAS User manual 2.6, http://adas.ac.uk, 2004.
[18] . https://open.adas.ac.uk.
[19] A. Foster. Ph.D. Thesis, University of Strathclyde, http://www.adas.ac.uk/theses/foster_thesis.pdf, 2008.
[20] F. Guzman*et al*. J. Phys. B At. Mol. Opt. Phys, 43:144007, 2010.
[21] R. L. Becker and A. D. MacKellar. J. Phys. B At. Mol. Phys, 12:L345, 1979.
[22] S. K. Rathgeber*et al*. Plasma Phys. Control. Fusion, 52:095008, 2010.
[23] R. S. Sutherland. Mon. Not. R. Astron. Soc., 300:321–330, 1998.
[24] T. Odstrcil *et al*. Rev. Sci. Instrum., 87.12:123505, 2016.
[25] T. Odstrcil *et al*. Nuclear Instruments and Methods in Physics Research Section A: Accelerators, Spectrometers, Detectors and Associated Equipment, 686:156–161, 2012.